Program Digest, 2019 IEEE International Ultrasonics Symposium (IUS)
Glasgow, Scotland, October 6-9, 2019

Contrast Mechanism of Ultrasonic-based Atomic Force Microscopy for Subsurface Imaging

Chengfu Ma
Department of Precision Machinery and Precision Instrumentation
University of Science and Technology of China
Hefei, China
chfuma@ustc.edu.cn

Yuhang Chen
Department of Precision Machinery and Precision Instrumentation
University of Science and Technology of China
Hefei, China
chenyh@ustc.edu.cn

Walter Arnold
Department of Materials Science and Engineering
Saarland University
Saarbrücken, Germany
arnoldwk@ieee.org

***Abstract*—Imaging of buried defects on a nanoscale is of significant importance for semiconductor devices and intracellular biological structures. In the last two decades, ultrasonic-based atomic force microscopy (AFM) has attracted intense attention as a surface mechanical characterization tool and is now commercially available. In this type of AFM mode, the eigenmodes of the cantilever are excited. Its amplitude, phase and eigenfrequencies are used as imaging quantities. Since its first introduction, several derivatives have been developed based on different ultrasonic excitation/detection schemes. Many successful applications have been carried out to measure local elastic and viscoelastic surface properties. Meanwhile, subsurface imaging using ultrasonic-based AFM is also shown to be possible by various groups. However, the contrast mechanism of subsurface ultrasonic AFM is not yet fully understood. This does not only prevent the evaluation of its detection capabilities, but also prevents accurate data interpretation and quantitative reconstruction of the subsurface object. The present study aims at understanding the contrast mechanism of subsurface ultrasonic AFM. Our results show that the contact stiffness variation is the key contrast mechanism for both subsurface cavity structures and embedded heterogeneous features. Applications of using ultrasonic AFM for detecting subsurface defects in graphite are also demonstrated.**

Keywords*—*ultrasonic atomic force microscopy, subsurface imaging, contrast mechanism, contact stiffness, defect

I. Introduction

Seeing below the surface is desirable in various fields. In nanotechnology, nondestructive subsurface metrology techniques are particularly important, for example, for imaging buried defects in semiconductor devices [1, 2] and intracellular structures [1, 3]. Facing this demand, ultrasonic-based atomic force microscopy (AFM) techniques have attracted intense attention. Since the first introductions by Rabe *et al* [4] and Yamanaka *et al* [5] two decades ago, several derivatives were developed based on different excitation/detection schemes. For instance, ultrasonic force microscopy (UFM) [5] and ultrasonic atomic force microscopy (UAFM) [6] apply ultrasonic vibrations to the AFM probe via the piezo built in the cantilever holder. Atomic force acoustic microscopy (AFAM) [4] excites the sample through a transducer beneath the sample. UFM is operated at frequencies much higher than the cantilever resonance, whereas UAFM and AFAM are operated at one of the cantilever's contact resonances (CRs), and together they are usually termed as CR-AFM. The later developed heterodyne force microscopy (HFM) [1, 7] excites both the probe and the sample at very high frequencies at MHz, and detects at the difference frequency, which is usually tuned to one of the CR frequencies.

These ultrasonic-based AFM techniques have been successfully applied for subsurface imaging in many fields. Examples are the observation of subsurface defects in highly oriented pyrolytic graphite (HOPG) [6, 8], the visualization of adhesion variations at buried interfaces [2], the detection of voids [9-11] and inclusions such as nanoparticles [1, 12] in semiconductor structures and advanced materials. Despite all the achievements, the physical imaging mechanism is still not fully understood. This prevents, on the one hand, the evaluation of the detection capabilities of the imaging setup and further its contrast optimization. On the other hand, accurate data interpretation and thus quantitative reconstruction of the subsurface features' properties become difficult. Quite a few efforts have been made to address this issue mainly from two points of view, respectively detecting the scattered near-field ultrasonic waves [13] and sensing the contact stiffness alterations [9-11, 14] induced by subsurface features.

In a recent study by us [15], we show that for imaging subsurface cavity structures using ultrasonic AFM, the induced contact stiffness variation is the key contrast mechanism. Here, we further extend this conclusion to embedded heterogeneous features. Applications of using ultrasonic AFM for subsurface defects detection are also demonstrated on a HOPG sample by visualizing grain boundaries and dislocations.

II. Subsurface Cavity Structures

We first explore the imaging contrast of ultrasonic AFM imaging for subsurface cavity structures. AFAM imaging was performed on a HOPG flake covering a Si substrate with open holes. The holes are fabricated by electron-beam lithography

This work was financially supported by the National Natural Science Foundation of China (Reference No. 51675504).

with various design diameters from approximately 2000 nm to 200 nm. HOPG flakes are cleaved using the scotch-tape method and transferred to the Si substrate. This technique yields subsurface cavities with well-defined lateral dimensions whose depths can be determined from the thicknesses of the covering flakes. In Figs. 1(a) and 1(b), we show respectively the topography and AFAM amplitude image taken near a HOPG flake. It can be found that the subsurface cavities covered by the flake are clearly revealed on the AFAM image. The flake is determined to have a mean thickness of 165 nm from the histogram of the topography. The experiments were carried out on a Dimension Icon AFM (Bruker, CA) with a commercial piezo disc (Steiner & Martins Inc., FL) as the sample transducer. A Multi75Al probe from BudgetSensors, Bulgaria was used, which has a calibrated spring constant of 3.48 N/m, using the thermal method and a natural frequency of 75.8 kHz. An operation frequency of 370 kHz and a tip load of 281 nN were used in imaging.

Moreover, halo-like features are observed for some of the cavities at their peripheries. We believe this indicates where resonance happens under the current operation frequency. To further explore this, AFAM experiments were performed with various operation frequencies from 380 to 345 kHz for the encased area in Fig. 1(b) which contains the largest cavity, a schematic of which is illustrated in the inset of Fig. 1(a). By using scanning electron microscopy, the diameter of the largest cavity was determined to be 1927 ± 22 nm. In Fig. 1(c), we show the resulting amplitude images. It can be found that, with decreasing operation frequency, a halo-ring appears at the periphery of the cavity which contracts and approaches the center. This can be understood by a gradual decrease of the contact stiffness sensed by the AFM tip from the periphery to the center and correspondingly a shift of the contact resonance of the AFM probe to lower frequencies. Therefore, resonance happens sequentially at different positions from the periphery to the center, while decreasing the operation frequency.

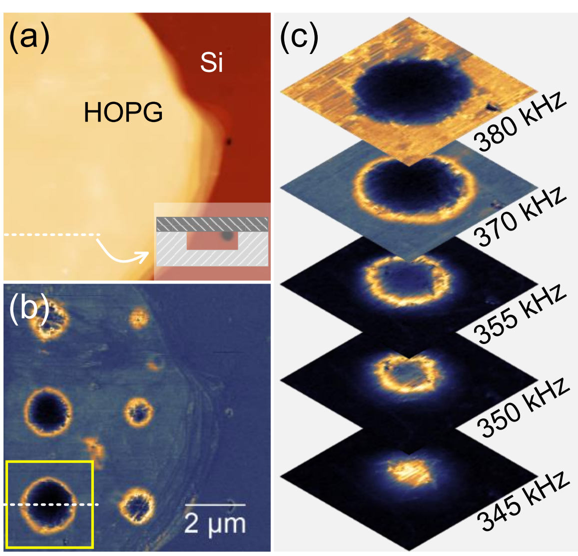

Fig. 1. (a) Topography and (b) AFAM amplitude image of a HOPG flake covering a Si substrate with open holes; (c) AFAM amplitude images of the encased area in (b) under various operation frequencies. A schematic illustration of the largest cavity is shown in the inset in (a).

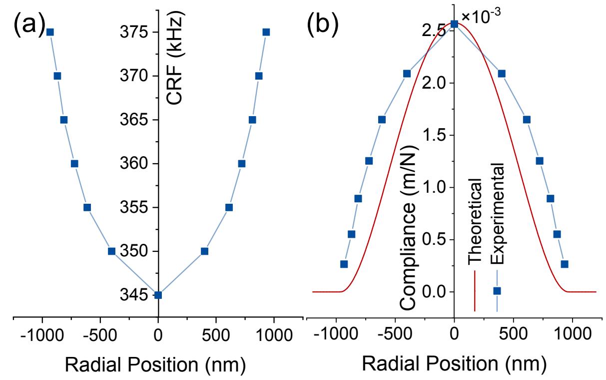

Fig. 2. (a) Relation between the resonance frequency and the position extracted from Fig. 1(c); (b) Experimental and theoretical compliance values at different positions of the cavity structure.

Quantitatively, we build from Fig. 1(c) the relationship between the resonance frequency and the corresponding position for the largest cavity, as shown in Fig. 2(a). Then, from the dispersion curve of the cantilever, we determine the contact stiffness from the resonance frequencies. Finally, by considering the measured contact stiffness above a cavity as a series connection of the deflection stiffness of the cavity structure and the material deformation stiffness, we obtain the deflection stiffness of the cavity structure, shown in Fig. 2(b) as its inverse counterpart, the compliance. We compare the results with a theoretical calculation of the compliance for a clamped circular plate by taking 1930 nm as the diameter and 165 nm as the thickness. It can be found that the experimental results agree well with the theoretical values. The calculations are based on models which can be found elsewhere [11, 15]. Parameters used for the cantilever model are: cantilever length L = 225 μm, cantilever tilt α_0 = 11°, tip height h = 17 μm, tip position L_1 = 215 μm. The ratio between the normal and lateral contact stiffness was assumed to be $\tau = k^*_{Lat} / k^* = 0.85$ [11, 15]. A Young's modulus and a Poisson's ratio value of (18 GPa, 0.25) are used for the HOPG sample. The above results strongly support that the induced contact stiffness variations are the contrast origins of ultrasonic AFM imaging for subsurface cavities.

III. Embedded Heterogeneous Features

Let us now consider the case of imaging subsurface features with heterogeneous mechanical properties. For this purpose, we produced samples by embedding SiO_2 particles with nominal diameters of 4 μm into a polydimethylsiloxane (PDMS) matrix. UAFM imaging was performed on a MFP-3D Origin AFM (Asylum Research, CA) by applying ultrasonic excitations through the piezo shaker built in the cantilever holder. A ContAl-G probe from BudgetSensors, Bulgaria, was used, which has a spring constant of 0.29 N/m and a natural frequency of 14.7 kHz determined by the thermal method. In Figs. 3(a) and (b), we show the topography and UAFM phase image taken with an operation frequency of 67 kHz and a tip load of 82 nN. It can be seen that many particles protrude in the topography image due to a matter of sample fabrication. It is further confirmed by the phase image that those particles visible in topography produce bull's eye features. The center part represents the bare SiO_2 particle (position 3) and the annulus the embedded part of the particle (position 2). An area with a diameter of approx. 2.5 μm was further examined, including the bare part with a diameter of approx. 0.85 μm. From a simple geometric calculation, we conclude that a detection depth of 390 nm was achieved for such particles. Moreover, it can also be observed that there are two particles which are not visible in the topography image, however, they are detectable in the phase image as indicated by the ellipses. Their phase contrast does not show the bull's eye features. This indicates that the particles are fully buried (position 4).

To investigate if the subsurface contrast comes from contact stiffness variations sensed by the AFM tip, force-distance curves above four different locations including the bare PDMS matrix (position 1) were taken as illustrated in the inset of Fig. 3(c). From the results shown in Fig. 3(c), it can be found that the force curve above the bare PDMS matrix is typical for soft materials, whereas the force curve above the bare SiO_2 particle is typical for rigid samples. However, force curves on both locations 2 and 4 coincide with each other and show a medium rigidity compared to the bare PDMS matrix and the SiO_2 particle. This proves that the stiffness variations induced by the embedded particles are indeed the origin of the contrast in the ultrasonic AFM images.

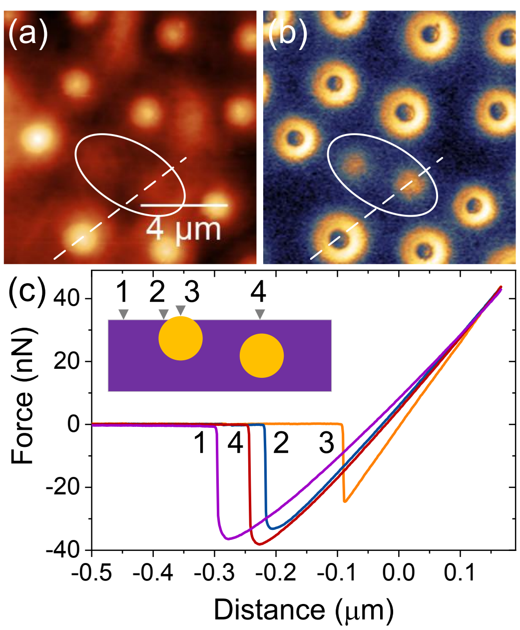

Fig. 3. (a) Topography and (b) UAFM phase image of embedded SiO_2 particles in a PDMS matrix; (c) Force-distance curves obtained above four positions as illustrated in the inset.

IV. Defect Imaging

Here we demonstrate applications of using ultrasonic AFM for defect imaging in a HOPG sample. UAFM imaging was first carried out on a HOPG sample, using a ContAl-G probe with an operation frequency of 72 kHz near its first contact resonance. The resulting topography and UAFM amplitude are shown in Figs. 4(a) and (b). It can be seen from Fig. 4(b) that, besides features resulting from the steps on the topography, clear domain structures can be observed which have sizes of around 20 - 30 μm. We believe that they are single-crystal grains in HOPG which usually have such sizes [16]. When we take a close look at the adjacent grains as encased in Fig. 4(b), a clear sharp grain boundary can be seen, as shown in the UAFM phase image in Fig. 4(c). Moreover, the observed dendritic features, which are topography steps, stop exactly at the boundary.

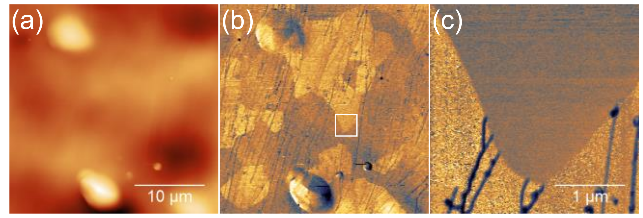

Fig. 4. (a) Topography and (b) UAFM amplitude image on a HOPG sample; (c) UAFM phase image of the encased area in (b).

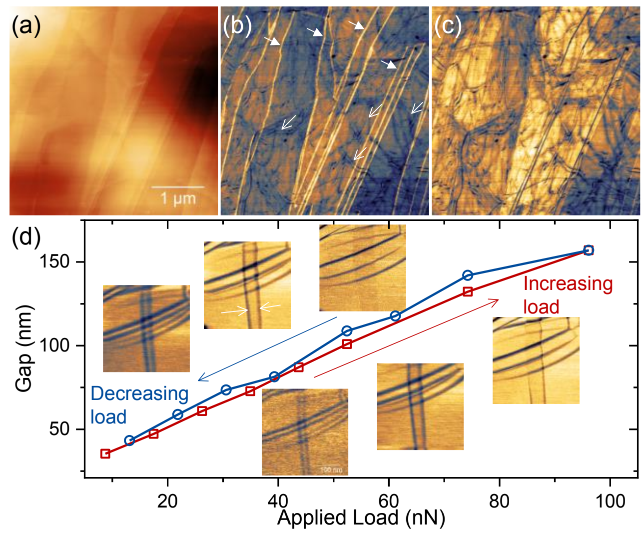

Fig. 5. (a) Topography and (b) (c) UAFM amplitude images of a HOPG sample. The operation frequencies are 216.5 kHz in (b) and 215.5 kHz in (c); (d) Relationship for the gap of a dislocation pair as a function of applied tip load. UAFM amplitude images for different tip loads are shown in insets.

Employing higher eigenmodes in ultrasonic AFM, usually leads to an increased sensitivity for stiffness changes on rigid samples, and thus benefits subsurface imaging. Deeper, smaller features are expected to be detected with higher eigenmodes [11]. To demonstrate this, we performed UAFM imaging on the HOPG sample with the operation frequency set close to the cantilever's second contact resonance. A ContAl-G cantilever was used. In Figs. 5(a) and (b), we show the resulting topography and UAFM amplitude image obtained with an operation frequency of 216.5 kHz. Bright linear-like features, indicated by arrows, are observed in the amplitude image which represent steps in the topography. Besides, many dark curved features which appear as twins can also be seen, as indicated by the white arrows. These features are not visible in the topography. We assume that they are subsurface edge dislocations as suggested earlier [6]. To visualize the dislocations more clearly, we shifted the operation frequency slightly to 215.5 kHz in order to reduce the sensitivity to topographical structures. The resulting UAFM image is shown in Fig. 5(c). Now features from the steps in the topography are hardly seen and the subsurface dislocations are clearly imaged. Such dislocations have been found to move reversibly in the lateral direction by changing the normal applied load [6]. As can be seen in the insets for some of the UAFM dislocation images, an increase and decrease of the applied tip load leads to reversible increase and decrease of the gap, recovering the original gap width. In Fig. 5(c) we explore this behavior further for a dislocation pair, see red (increasing load) and blue curves (decreasing load). There is an almost linear relation between the gap width and the applied load with no hysteresis after the load is reduced to zero. Its slope is ≈ 1.42 nm/nN. This is different from the value in [6], where a value 0.25 nm/nN was found. We suggest that the difference results from a different depth of the dislocations or a different force resisting their sliding in the interlayer where the dislocations are located, however further investigations are needed which are beyond the scope of the present work.

V. Conclusion

The physical contrast mechanism of using ultrasonic AFM for subsurface imaging has been investigated. The results show that for both subsurface cavity structures and embedded heterogeneous features, the contact stiffness variations induced by them are the key contrast origin. Ultrasonic AFM imaging of defects, such as grain boundaries and subsurface dislocations, is also demonstrated.

References

[1] G. S. Shekhawat and V. P. Dravid, "Nanoscale imaging of buried structures via scanning near-field ultrasound holography", Science, vol. 310, 89-92, 2005.

[2] D. C. Hurley, M. Kopycinska-Müller, E. D. Langlois, A. B. Kos, and N. Barbosa III, "Mapping substrate/film adhesion with contact-resonance-frequency atomic force microscopy", Appl. Phys. Lett., vol. 89, 021911, 2006.

[3] L. Tetard, A. Passian, and T. Thundat, "New modes for subsurface atomic force microscopy through nanomechanical coupling", Nat. Nanotechnol., vol. 3, 105-109, 2008.

[4] U. Rabe and W. Arnold, "Acoustic microscopy by atomic force microscopy", Appl. Phys. Lett., vol. 64, 1493-1495, 1994.

[5] K. Yamanaka, H. Ogiso, and O. Kolosov, "Ultrasonic force microscopy for nanometer resolution subsurface imaging", Appl. Phys. Lett., vol. 64, 178-180, 1994.

[6] T. Tsuji, and K. Yamanaka, "Observation by ultrasonic atomic force microscopy of reversible displacement of subsurface dislocations in highly oriented pyrolytic graphite", Nanotechnology, vol. 12, 301-307, 2001.

[7] M. T. Cuberes, H. E. Assender, G. A. D. Briggs, and O. V. Kolosov, "Heterodyne force microscopy of PMMA/rubber nanocomposites: nanomapping of viscoelastic response at ultrasonic frequencies", J. Phys. D: Appl. Phys., vol. 33, 2347-2335, 2000.

[8] T. Wang, C. Ma, W. Hu, Y. Chen, and J. Chu, "Visualizing subsurface defects in graphite by acoustic atomic force microscopy", Microsc. Res. Techniq., vol. 80, 66-74, 2017.

[9] Z. Parlak and F. L. Degertekin, "Contact stiffness of finite size subsurface defects for atomic force microscopy: Three-dimensional finite element modeling and experimental verification", J. Appl. Phys., vol. 103, 114910, 2008.

[10] A. Striegler, B. Koehler, B. Bendjus, M. Roellig, M. Kopycinska-Mueller, and N. Meyendorf, "Detection of buried reference structures by use of atomic force acoustic microscopy", Ultramicroscopy, vol. 111, 1405-1416, 2011.

[11] C. Ma, Y. Chen, W. Arnold, and J. Chu, "Detection of subsurface cavity structures using contact-resonance atomic force microscopy", J. Appl. Phys., vol. 121, 154301, 2017.

[12] K. Kimura, K. Kobayashi, K. Matsushige, and H. Yamada, "Imaging of Au nanoparticles deeply buried in polymer matrix by various atomic force microscopy techniques", Ultramicroscopy, vol. 133, 41-47, 2013.

[13] H. J. Sharahi, G. S. Shekhawat, V. Dravid, S. Park, P.Egberts, and S. Kim, "Contrast mechanisms on nanoscale subsurface imaging in ultrasonic AFM: scattering of ultrasonic wave and contact stiffness of tip-sample", Nanoscale, vol. 9, 2330-2339, 2017.

[14] A. Yao, K. Kobayashi, S. Nosaka, K. Kimura, and H. Yamada, "Visualization of Au nanoparticles buried in a polymer matrix by scanning thermal noise microscopy", Sci. Rep., vol. 7, 42718, 2017.

[15] C. Ma, W. Wang, Y. Chen, W. Arnold, and J. Chu, "Depth-sensing using AFM contact-resonance imaging and spectroscopy at the nanoscale", J. Appl. Phys., in press.

[16] J. Avila and M. C. Asensio, "First nanoARPES user facility available at SOLEIL: an innovative and powerful tool for studying advanced materials", Synchrotron Radiation News, vol. 27, 24-30, 2014.